Journal of Fluids and Structures 18 (2003) 3–22

JOURNAL OF
FLUIDS AND
STRUCTURES

www.elsevier.nl/locate/jnlabr/yjfls

Nonlinear effects in transonic flutter with emphasis on manifestations of limit cycle oscillations

G. Schewe*, H. Mai, G. Dietz

Institut für Aeroelastik des DLR, Bunsenstr. 10, D-37073 Göttingen, Germany

Received 31 October 2002; accepted 3 July 2003

Abstract

This paper presents flutter and forced oscillation experiments in a transonic wind tunnel. For an aeroelastic supercritical 2-D airfoil configuration we studied typical transonic phenomena in as pure a form as possible. Various manifestations of small-amplitude limit cycle oscillations were observed for different flow conditions as well as coexisting limit cycles. We demonstrated how very small control forces were sufficient to excite or suppress flutter oscillations. Limit cycle oscillations occurred under free and forced turbulent boundary layer transition in a perforated wall test-section. Flutter calculations based on experimental aerodynamic forces yield stability limits which show good agreement with directly measured experimental flutter values. The results indicate that flow separation at the trailing edge, and the interactions between the shock and the marginal region of separated flow beneath it, may be responsible for limiting the amplitude of the observed limit cycle oscillations.

1. Introduction

Flutter of an aircraft wing is an aeroelastic phenomenon that may occur above a critical dynamic pressure. In the transonic flow region, it is commonly observed that there is a significant reduction of this critical dynamic pressure for flutter onset. Furthermore, instead of exponentially divergent behaviour being observed, typically the coupled structural/fluid-dynamic instability evolves into a limit cycle oscillation (LCO). This LCO behaviour is attributed to the fact that the relative flow speeds are close to the propagation speeds of the infinitesimal disturbances, thus leading to nonlinear effects such as compression shocks. In addition, instabilities can occur within the airfoil's boundary layer and, via interactions with the laminar-turbulent transition process, lead to flow separations. The formation of fluid-mechanical structures, or more generally, changes in the topological structures of separated flows, are intrinsically nonlinear. All of these effects can undergo mutual interactions and are, therefore, sources of extreme nonlinear behaviour. The nonlinearity of the flow is thus the dominant feature of transonic flutter. Evidence for this is the appearance of limit cycle oscillations in transonic flutter. The mechanisms behind the amplitude limitation are currently not fully understood. Many questions still remain open: The role of laminar-turbulent boundary-layer transition is still unclear. Limit cycle oscillations of relatively small amplitudes might be artefacts of the wind-tunnel experiment. Furthermore, the aerodynamics responsible for the amplitude-limiting process could not be satisfactorily identified.

Up to the present time, there have been few reported experimental investigations of nonlinear effects in transonic flutter. The study by Rivera et al. (1992) presents experimental flutter data for a rigid, single-side mounted semi-span model of a NACA 0012 airfoil having two degrees of freedom and low aspect ratio. They present a time history showing scale-less sinusoidal pitch and plunge flutter motions that are amplitude limited, but they do not discuss the amplitude limitation. To the best of our knowledge, for the two-dimensional case in a two-sided elastic suspension system the first

---

*Corresponding author. Tel.: +49-551-709-2423; fax: +49-551-709-2862.
E-mail address: guenter.schewe@dlr.de (G. Schewe).

0889-9746/$ - see front matter © 2003 Elsevier Ltd. All rights reserved.
doi:10.1016/S0889-9746(03)00085-9

Nomenclature

a_∞	speed of sound in the incident flow (inflow)
b	span width
c	chord of airfoil
c_l	$L/(q_\infty cs)$, lift coefficient
c_m	$M/(q_\infty c^2 b)$, moment coefficient
D_α	torsion damping
D_h	heave damping
Fi	Flutter index
f	frequency
h	deflection in the direction of lift
Δh	amplitude of the heave oscillations
I_α	moment of inertia
K_α	torsion spring-stiffness constant
K_h	heave spring-stiffness constant
L	lift
M	moment around $c/4$, positive in the clockwise direction
MP	measuring point No.
Ma_k	corrected Mach number of the inflow
Ma_u	uncorrected Mach number of the inflow
m	mass
p_∞	static pressure of the inflow
p_0	stagnation pressure of the inflow
q_∞	$1/2\ \rho_\infty u_\infty^2$ dynamic pressure of inflow
Re	Reynolds number
r_α	radius of gyration
S_α	static unbalance
T_∞	static temperature
U_∞	free stream velocity
x	spatial coordinate in the stream wise direction
X_α	$\partial x/\partial\alpha_0$, partial derivative
x_α	static unbalance (dimensionless)

Greek Letters

α_0	initial angle of attack without wind, positive in the clockwise direction
α_k	corrected angle of attack
α_u	uncorrected angle of attack
$\Delta\alpha$	amplitude of pitching oscillations
δ_α	Lehr's pitch-damping coefficient
δ_h	Lehr's plunge-damping coefficient
κ	adiabatic constant $= 1.4$ (ratio of specific heats)
μ	mass ratio
ρ_∞	free stream density
ρ_m	total mass density
ω	$2\pi f$, circular frequency
ω^*	$\omega c/u_\infty$, reduced frequency
ω_α^*	uncoupled circular pitching frequency
ω_h^*	uncoupled circular heave frequency

clear observations and measurements of several types of such amplitude-limited oscillations were made in our exploratory experiments described by Schewe and Deyhle (1996). These experiments were conducted using a supercritical NLR 7301 airfoil (Zwaan, 1979). The aerodynamic properties of this NLR 7301 airfoil were the subject of detailed experiments reviewed by Tijdeman and Seebass (1980), including steady and unsteady pressure measurements as well as visualization of the flow over a steady or oscillating NLR 7301 airfoil. The continuation of our heave/pitch flutter experiments using the NLR 7301 airfoil in transonic flow was described by Knipfer and Schewe (1999) and Schewe et al. (2002). They conducted a test case known as MP 77 that was the subject of several numerical investigations. This test case will be reviewed and discussed in detail in the present paper.

Numerical studies of transonic flutter have been reported by several authors, including Bendiksen (1989) and Schulze (1997), who made use of the Euler equation and found such nonlinear effects as LCOs. Bendiksen (1989) simulated, described and discussed phenomena such as LCOs, weak divergence and flutter-divergence interaction. Weber et al. (2001) and Tang et al. (2001) used a thin layer Navier–Stokes solver to simulate the test case MP 77 from Knipfer and Schewe (1999) and Schewe et al. (2002). In both investigations LCOs were found for the same structural and nearly the same flow conditions. However, the predicted LCO amplitudes are also rather high compared to the experimental observations. Weinman and Günther (2002) integrated the complete Navier–Stokes equations using a very high spatial and temporal resolution and found smaller LCO amplitudes than in both aforementioned papers; however, the amplitudes are still much higher than the ones found experimentally. Thomas et al. (2002) using a harmonic balance method studied the behaviour of the aeroelastic system at flow conditions in the vicinity of the test case MP 77 and were able to compute complete bifurcation diagrams, which also showed rather large LCO amplitudes.

The reason for the discrepancy between the numerical and experimental data is not yet well understood. A possible explanation could be the existence of multiple LCOs, i.e., coexisting LCOs at constant flow conditions, which will be described in the present paper. The investigation of Weber et al. (2001) has been continued by Castro et al. (2001) who took into account the presence of the porous wind-tunnel walls by appropriate boundary conditions in their computational model. Their numerical results show that the value of the LCO amplitude is significantly affected by the porosity of the walls. The porosity has a strong impact to the simulated LCO amplitudes while the flutter frequency and the phase relation between heave and pitch is nearly unaffected. Although the wind-tunnel wall boundary condition significantly influences the flutter characteristics, in Schewe et al. (2002) we have shown that in a similar adaptive test-section with solid nonporous walls LCOs with relatively small amplitudes $<1^\circ$ still occur.

In the present paper we report the results obtained in flutter and forced oscillation experiments of a rigid NLR 7301 airfoil in transonic flow. A two-dimensional model is more easily suited for computational comparison purposes than a three-dimensional one, since the flow is less complex in the former case than in the latter. The applied airfoil model can be assumed to exhibit a rigid body motion in two degrees of freedom, since it was elastically suspended on both sides as symmetrically as possible. This mounting problem is obviously the reason why so few two-dimensional experiments have thus far been carried out. The flutter test set-up was first described in Schewe and Deyhle (1996). Some results of a second block of flutter and forced oscillation experiments in pitch and plunge using a model equipped with pressure transducers were presented in Knipfer and Schewe (1999). Up to this time, laminar-turbulent boundary-layer transition over the model's surface was allowed to develop without any artificial tripping. In Knipfer and Schewe (1999) a test case MP 77 was presented. The present paper contains further results in the context of this MP 77 like unsteady pressure distributions during flutter and forced oscillations. In addition results of a third block of experiments are presented, where the boundary-layer transition has been tripped. All of these experiments were performed in the test-section with porous walls. The major goals of the present investigation can be summarized as follows: (i) locating manifestations of LCOs, (ii) answer the question, whether the oscillation amplitudes always remain small? (iii) provide experimental data for validation of numerical simulations, i.e., supply benchmark test cases.

2. Experimental arrangement

2.1. The Transonic Wind Tunnel Göttingen (TWG)

The experiments were carried out in the Transonic Wind Tunnel Göttingen (TWG), which has a test-section cross-section of $1\,\mathrm{m} \times 1\,\mathrm{m}$ and is built for continuous operation. The experiments were conducted in the test-section outfitted with perforated walls. The perforation holes account for 6% of the total test-section wall surface area, and the holes are inclined at an angle of 30° to the direction of the flow. Since the far-field boundary conditions in the perforated test-section do not correspond to free-flight conditions, appropriate wind tunnel wall effects corrections, as described by Schewe et al. (2002) are made. The question about necessary corrections of the angle of attack and the Mach number will be discussed in the context of the test cases in Section 3.3.

2.2. The flutter-test set-up and model

Fig. 1 shows a schematic representation of the experimental flutter-test set-up. An airfoil model having a chord of $c = 0.3\,\mathrm{m}$ and a span of $s = 1\,\mathrm{m}$ is elastically mounted with two degrees of freedom in the flutter test set-up. The geometry

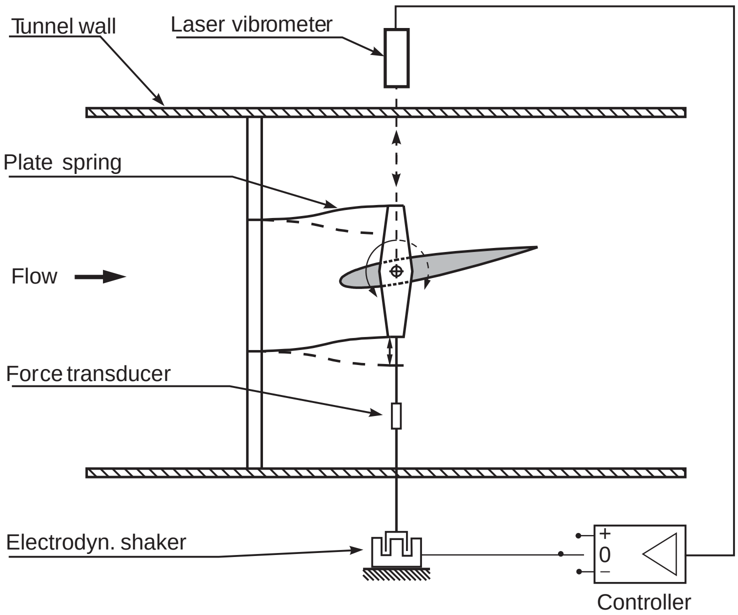

Fig. 1. Side-view sketch of the experimental configuration for self-excited oscillations of an airfoil in two degrees of freedom, heave (h) and torsion (α). The laser vibrometer, electrodynamic exciter and controller form the flutter control system.

of the model corresponds to that of a supercritical NLR 7301 airfoil (Zwaan, 1979). The relatively high thickness of this airfoil is convenient for getting a stiff model. The mounting fixture on both sides of the model consists primarily of a bending and a torsion spring. After the fixture has been tuned, it provides a nearly symmetrical mounting for the model. The model combines light weight with a high stiffness since it is made of carbon-fibre composite. Measurements were performed with free and forced laminar/turbulent boundary-layer transition (tripped with zigzag band: suction side $x/c = 0.3$; height: 0.3 mm; pressure side $x/c = 0.07$; height: 0.1 mm).

To measure the steady and unsteady forces, a piezoelectric balance described by Schewe (1991) was installed on each side of the model in between the bending and the torsion springs. For measurement of steady and unsteady pressures, 80 miniature differential pressure sensors were installed beneath the surface of the model, 40 in the midspan section, and 40 in the side section ($c/2$ apart in lateral direction).

The model's axis of rotation was always at 25% of the chord. On both sides, the angle of attack and the heave displacement of the airfoil was measured using two laser triangulators at each side—one forward of the shaft and one behind it. The data provide the instantaneous heave $h(t)$ and angle of attack $\alpha(t)$ of the airfoil. One or both types of springs could also be blocked, independent of one another. By blocking only the torsion springs and coupling the bending springs on either side of the model with a hydraulic linear actuator, we could then forcibly excite heave oscillations.

In case of flutter experiments, a pneumatic friction brake could be attached, acting as a mechanical flutter stopper, when a pre-selected threshold amplitude of the angle of attack, typically 2°, was exceeded.

2.3. The flutter-control system for the flutter test set-up

Fig. 1 also shows a schematic representation of the flutter-control system used to dampen or excite oscillations of the model. A laser vibrometer was used to measure heave displacement and velocity of the airfoil oscillations. The measuring point was located mid-span at the axis of rotation so that only the heave motion was measured. The heave-speed signals were fed into an operational amplifier and then into one electrodynamic exciter at each side. The excitations act directly on the bending springs in the heave direction, whose connecting box forms the basis for the piezoelectric balance. Thus the excitation forces do not act directly on the piezoelectric balance, but, rather, appear only indirectly in the balance signals since the heave motion of the airfoil induces inertial forces. The exciter force F_z itself was measured directly (see Fig. 1) with the piezoelectric force sensor built into the heave rod.

If the signals were fed directly into the electrodynamic exciters, small motions of the model would be amplified or excited because of the positive feedback. If the signals were inverted (negative feedback) then self-excited oscillations of the model could be damped. In the figures for the following sections, time ranges with positive feedback are identified by (+), those with negative feedback by (−), and those where the control device was open (no feedback) by (0).

2.4. Theoretical model of the structural dynamics

Fig. 2 sketches a theoretical model of the structural dynamics of the test set-up configuration with the two degrees of freedom, i.e., heave and pitch. The equation of motion based on the model in Fig. 2 can be written as

$$\begin{bmatrix} 1 & -x_\alpha \\ -x_\alpha & r_\alpha^2 \end{bmatrix} \frac{\partial^2 \mathbf{q}(t^*)}{\partial t^{*2}} + 2\begin{bmatrix} \delta_h \omega_h^* & 0 \\ 0 & r_\alpha^2 \delta_\alpha \omega_\alpha^* \end{bmatrix} \frac{\partial \mathbf{q}(t^*)}{\partial t^*} + \begin{bmatrix} \omega_h^{*2} & 0 \\ 0 & r_\alpha^2 \omega_\alpha^{*2} \end{bmatrix} \mathbf{q}(t^*) = \frac{2}{\pi\mu} \begin{bmatrix} c_l(t^*) \\ c_m(t^*) \end{bmatrix},$$

where

$$\mathbf{q}(t^*) = \begin{bmatrix} h^*(t^*) \\ \alpha(t^*) - \alpha_0 \end{bmatrix}.$$

This equation describes the changes of the nondimensional heave $h^*(t) = h(t)/c$ and the difference between the instantaneous angle of attack $\alpha(t)$ and its off-wind value α_0, as a function of the nondimensional time $t^* = tu_\infty/c$. Other dimensional parameters are the chord length c, the mass m, the static unbalance S_α, the moment of inertia I_α, the spring-stiffness constants $K_{\alpha/h}$, the dampings $D_{\alpha/h}$, the incident flow speed u_∞, and the freestream density ρ_∞. The nondimensional structural parameters are then defined as:

static unbalance $x_\alpha = S_\alpha/(mc)$,

radius of gyration $r_\alpha = \sqrt{I_\alpha/(mc^2)}$,

uncoupled circular pitching frequency $\omega_\alpha^* = \sqrt{K_\alpha/I_\alpha}c/u_\infty = \omega_\alpha c/u_\infty$,

uncoupled circular heave frequency $\omega_h^* = \sqrt{K_h/m}c/u_\infty = \omega_h c/u_\infty$,

Lehr pitching damping $\delta_\alpha = D_\alpha/(2\sqrt{K_\alpha I_\alpha})$,

Lehr heave damping $\delta_h = D_h/(2\sqrt{K_\alpha m})$.

The mass ratio $\mu = m/[(\pi/4)\rho_\infty c^2 b] = \rho_m/\rho_\infty$ characterizes the ratio of aerodynamic to structural inertial forces by ρ_m, the total density of the mass undergoing heave oscillations, where the mass is relative to the reference volume $\pi(c/2)^2 b$.

The parameters for the chord length, mass, and torsion-spring stiffness were determined from direct measurements. The following direct measured values (Table 1): moment of inertia, the static unbalance and the bending-spring stiffness were measured but corrected using the results of a ground vibration test. The corrections minimized the deviations of the measured to the theoretically obtained eigenfrequencies and maximized the parallelism of the eigenvectors of the

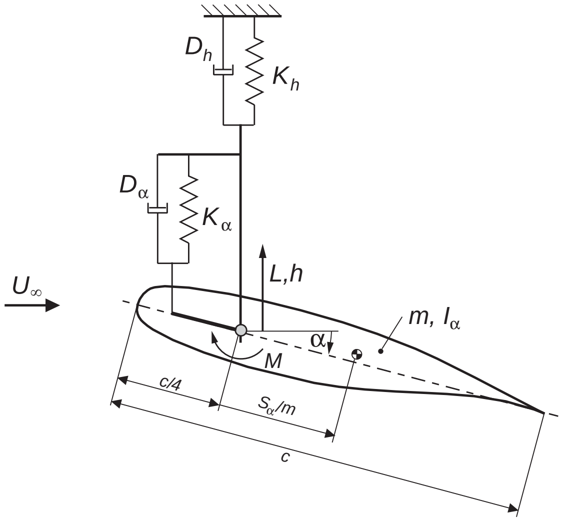

Fig. 2. Model of the structural dynamics.

Table 1
Flutter parameters from Schewe et al. (2002)

x_α	r_α	$\omega_\alpha(1/\mathrm{s})$	$\omega_h(1/\mathrm{s})$	ω_h/ω_α	δ_α	δ_h	ρ_m (kg/m^3)
0.0484	0.197	271.9	206.6	0.761	0.41%	0.73%	366.9

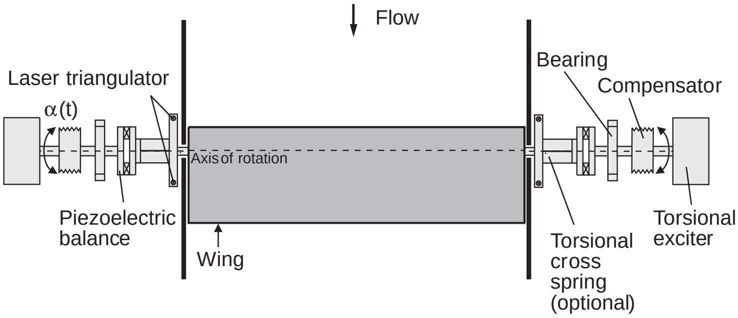

Fig. 3. Pitch test set-up for forced torsion oscillations. The installation of both optional torsion springs (cross springs) gives the wing a torsion degree of freedom for investigating torsional flutter—not applied here.

model motion to those determined by measurement. The deviations of the eigenfrequencies of the structural-dynamical model (using the corrected parameters and without it being encumbered by aerodynamic loads) from those obtained from ground vibration tests, are smaller than 0.4%, and the parallelism of the eigenvectors is greater than 99.8%. The values for the Lehr's damping were taken from the ground vibration tests. Table 1 lists the flutter parameters.

2.5. Test set-up for forced pitch oscillations

A schematic representation of the test set-up for forced pitch oscillations is shown in Fig. 3. The angle of attack of the model can be varied by ±10° via two hydraulic rotation actuators operated in phase opposition. Since we could generate forced pitching oscillations up to a frequency of 60 Hz, reduced frequencies of nearly 0.5 are possible. In addition to the rotation actuators, the symmetrical suspension system comprised a compensator, a bearing, the piezoelectric balance, and a slat acting as a reference base for position measurements by four laser triangulators similar to the configuration of our flutter test set-up.

3. Results

Two kinds of experiments were conducted: The flutter test set-up has been used to detect the flutter-stability boundary and to investigate limit cycle oscillations. Forced oscillation experiments yield the aerodynamic response to harmonic motions of the airfoil. The results of the latter measurements have been used to analyse the stability of the equation of motion from Section 2.4 in order to compare these results with the experimentally obtained flutter boundary. In the following, flutter onset results are presented before various manifestations of LCOs are described. A LCO experiment is also proposed as a test case for comparison with numerical simulations. Afterwards, the aerodynamic response to forced heave and pitch oscillations including its amplitude dependency is depicted.

3.1. Procedure for direct flutter measurements and stability limit detection

The first goal when making flutter measurements is to establish the stability boundary, which depends upon the Mach number, the angle of attack α, structural properties of the model, mass ratio, and dynamic pressure. If we want to investigate how stability depends on these parameters when α is constant, we have to compensate for changes in the angle of attack α, caused by variations in the dynamic pressure. We accomplished this in our experiments by selecting an appropriate off-wind value of the angle of attack α_0 resulting in the aimed mean angle of attack α under air load.

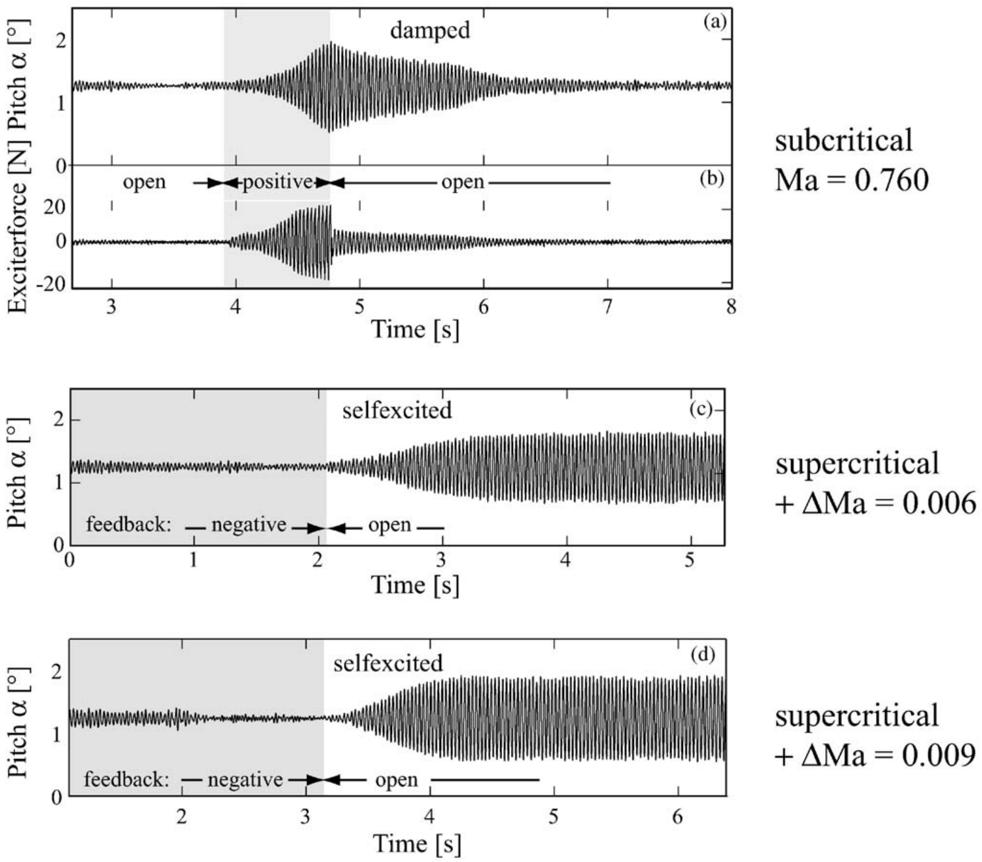

Fig. 4. Time histories of the angle of attack $\alpha(t)$ in the vicinity of a critical Mach number. The curve in (b) represents the exciter force corresponding to the subcritical case in (a). Case (c), i.e., MP 224 and (d) are supercritical (see also Table 3).

The flutter measurements were carried out for the Mach number range $0.5 < \mathrm{Ma} < 0.92$, and the stagnation pressure was varied within the range $0.35 < p_0 < 0.8$ bar. By means of Fig. 4 we will depict how the critical points (the onset of flutter) in the transonic region were sought and located.

The suspected stability boundary was approached by stepwise increases in the Mach number, while the control device was switched to negative feedback (= damping). After each step, the control device was turned off (feedback = 0) for a short time. Then, by observing the time histories of $\alpha(t)$ and heave $h(t)$, we could determine whether a self-excited state existed or not. Small disturbances that can initiate crossover are always present, e.g., fluctuations in the incident flow. The flow Mach number (at constant stagnation pressure) at which self-excitation first appears, can be regarded as being very near the flutter onset condition.

In principle, the flutter boundary can also be determined at a constant Mach number and appropriate stagnation pressure variations. The Mach number variations preferred by us have the advantage that they allow faster but relatively small changes.

To make clear the behaviour in the vicinity of the critical state, three examples shall be discussed, which in the case of limit cycle oscillations involve the heaving and pitching modes.

Fig. 4 shows three α-signals, one at a subcritical Mach number (a), and two at supercritical Mach numbers (c,d). The curve in (b) represents the simultaneously measured force in the exciter rod belonging to case (a). We see from the exciter-rod-force signal (b) that the control device was switched to positive feedback (+) within the labelled time span, and the artificially excited oscillations are shown in (a). After the control device is switched off (open loop) at $t = 4.8$ s, the oscillations decay, i.e., the system is damped and thus in a subcritical state. In the supercritical cases (c,d), no external excitation is necessary—after the control device is opened, the heave and pitching flutter oscillations begin and subsequently evolve into limit cycle oscillation in heave and pitch with a phase shift $\Delta\varphi$ of almost 180°. The increase in Mach number ($\Delta\mathrm{Ma} = 0.003$) from case (c) to case (d) has the consequence that the growth rate as well as the limit cycle amplitude is distinctly higher. In other words, the limit cycle in case (d) is reached in a significantly shorter time. In the later Fig. 13 (also in Table 3), the growth rates and the LCO amplitudes are shown for various Mach numbers.

Fig. 5 shows a stability diagram for two mean angles of attack $\alpha \approx 1.25^\circ$ and $\alpha \approx 0.25^\circ$, which, in a restricted sense, have to represent a narrow range of angles, where the data points at the transonic Mach numbers were determined using the procedure described above. The reason for the scattering of the mean angle of attack is that α adjusts itself according to the static aeroelastic equation depending on the particular flow state. Therefore, we selected the results of measurements made at different pre-set off-wind angles of attack α_0 at which the different angles of attack adjusted by the dynamic pressure were close to having the same value.

To determine the stability boundary at Mach numbers below those in the transonic dip region, another method was chosen. In this instance, we set Ma = const. and determine the stagnation pressure where flutter onset occurs. Specifically a combination of preset angle α_0 and stagnation pressure was selected in such a way that the resulting mean angles of attack adjusted by the different stagnation pressures p_0 had approximately the same value. With an increase in the stagnation pressure and the accompanying approach to the stability boundary, the frequencies of the heave and pitch modes approach one another. From the magnitude and proximities of the two frequencies, the value of the flutter point can be determined using Zimmerman–Weissenburger's extrapolation criterion (1964). The three so-determined subsonic flutter points are indicated in the stability diagram in Fig. 5 as open circles. These data, as well as those labelled 1.K in Fig. 5, can be found in dimensional units in Schewe and Deyhle (1996).

Fig. 5 shows directly determined flutter points in the form of a nondimensional flutter index $\mathrm{Fi}=u_F^*/(\mu)^{1/2}$ where $u_F^* = 2u_\infty/(c\omega_\alpha)$. The flutter index represents a nondimensional dynamic pressure (ratio of the aerodynamic loads to the structural stiffness). As the Mach number approaches transonic values, the stability boundary first decreases, then increases again beyond the minimum of the transonic dip. When the angle of attack is decreased, the nadir of the dip is shifted to higher Mach numbers and the dip region becomes broader.

The results of corresponding flutter calculations, based on experimentally measured responses of the unsteady aerodynamic loads to forced heave and pitch oscillations, are also shown in Fig. 5. These flutter calculations determine the flutter boundary as the stability limit of the equation of motion assuming harmonic motions that induce harmonic airloads. Within the calculation the reduced frequency as well as the mass ratio are varied until neutral damping of the aeroelastic system is found for a set of given inflow parameter. In addition a result of a flutter calculation based on Theodorsen's analytical unsteady incompressible aerodynamic solution is included in Fig. 5, showing that for low Mach numbers our results are consistent with classical methods. Around Ma = 0.75, where the measured flutter speed index decreases significantly, as well as the experimentally obtained location and depth of the minimum flutter speed index at Ma = 0.77, are both reproduced well by the calculated curve. The reason for any differences can most likely be attributed to the considerable scatter of the mean angle of attack during the measurements of the experimentally determined unstable points.

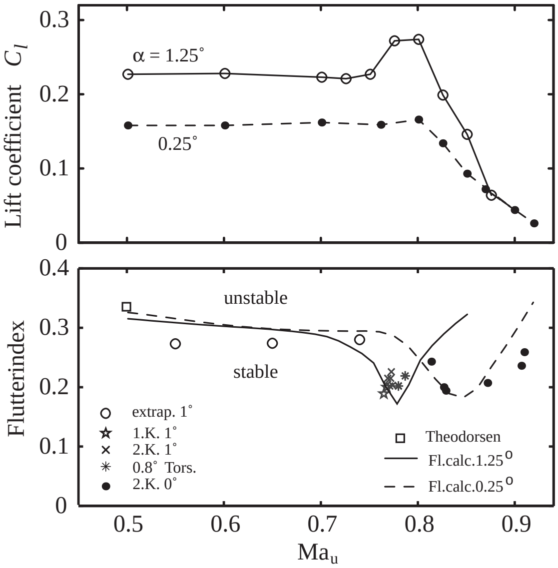

Fig. 5. Stability diagram (free transition) for two mean angles of attack. The upper part of the figure shows the corresponding curves of the lift coefficient at stationary flow conditions (1.K.: 1. test block Schewe and Deyhle (1996), 2.K.: 2. test block).

Table 2
Flow and structural parameters as well as LCO properties at distinct measuring points. More MPs in Schewe et al. (2002)

	Flow and structural parameters								LCO properties						
MP	Ma_u	Re ($\times 10^6$)	T_∞ (K)	U_∞ (m/s)	ρ_∞ (kg/m^3)	μ	Fi	α_0 (°)	α_u (°)	c_l	c_m	h_{LCO} (mm)	α_{LCO} (°)	$\Delta\varphi$ (°)	ω_F^*
77	0.768	1.7	274	255	0.388	942	0.204	1.9	1.28	0.272	−0.082	0.75	0.2	176	0.242
859	0.820	2.4	271	270	0.497	745	0.245	1.0	0.33	0.160	−0.065	1.72	0.31		0.228

The two computed flutter curves, one for $\alpha = 1°$ (lower Mach number dip) and one for $\alpha = 0°$ (higher Mach number dip) in Fig. 5, represent two different cases, which is made clear by the curves of the lift coefficients (upper part of Fig. 5) that were determined by separate stationary measurements in the test set-up for forced pitch oscillations (Fig. 3). Since the effective angle of attack varies somewhat during the flutter measurements, the connection between the sets of curves should not be over-interpreted. Nevertheless, it is obvious that for a mean angle of attack in the range of $\alpha = 1°$ (lower Mach number dip) the minimum of this flutter speed onset dip lies at just about the same Mach number at which the mean aerodynamic lift attains a maximum.

Table 2 gives a list of two characteristic unstable measuring points and the accompanying, relevant parameters for the flow and structure.

3.2. *Manifestations of limit cycle oscillations in transonic flow*

Schewe and Deyhle (1996) have reported various types of limit cycle oscillations at free transition, observed near the minimum of the transonic dip. Limit cycle oscillations in both the heave and torsion mode, pure amplitude-limited pitching oscillations and alternating excitations of the heave and pitching modes were found.

In the following, we present manifestations of limit cycle oscillations at forced transition. In addition to the transition strip, a very small removable contour bump was applied to the model for the experimental results shown in Figs. 6–12. This was done in order to reduce the strength of the suction-side shock and thus to reduce the wave drag. For the cases shown here, however, the bump did not greatly effect the wave drag because at the low angle of attack investigated, the shock location differs from the bump position.

Fig. 6 demonstrates typical properties of LCOs and their response to small external excitations—acting only on the heave mode—slightly above the stability boundary. Up to time $t = 1.6$ s, the control device was switched to negative feedback (= flutter/LCO suppression). After opening the control loop (zero feedback) the system would oscillate freely with a relatively low limit cycle amplitude. When positive feedback was switched on at $t = 7.3$ s, the amplitude of the limit cycle amplitude more than doubled. After opening the loop again at $t = 13.3$ s (i.e., zero feedback), the system returns to the same limit cycle amplitude as before. At $t = 18.8$ s, the signal of the exciter force is overshooting since negative feedback was switched on, consequently the oscillations were almost completely suppressed. Thus it is demonstrated that the system returns to the same limit cycle amplitude regardless of the starting condition.

As it turned out, we were able to control the state of the system with very small forces. This characteristic also becomes clear in the following Figs. 7 and 8, in which the transitions are artificially initiated. For comparison, in addition to the excitation force, these figures also show the temporal behaviour of the lift. The necessary excitation forces are typically two orders of magnitude smaller than the lift forces that appear.

It can be seen in Fig. 7 how a small disturbance can provoke a discontinuous transition to a limit cycle with amplitude of about 0.5° in pitch. After about 2 s the amplitude, under otherwise constant conditions, jumps from this level to a somewhat higher one. Obviously there are two neighbouring states—the first one less stable compared to the second state.

The effect of the flutter-control device can be seen very clearly at $t = 22$ s. There the system is switched to negative feedback and the oscillations are suppressed in both modes, although only the heave mode is controlled.

In the next experiment, the Mach number was increased by a very small amount, only $\Delta Ma = 0.003$. Figs. 8 and 9 demonstrate the existence, under constant flow conditions, of multiple limit cycles, coexisting in phase space, and which are clearly distinct from one another. These limit cycles were reached via very small disturbances at $t = 6$ and 11 s, respectively. It can be seen in Fig. 9 that the aeroelastic system exhibits greater nonlinearity in the pitching motion $\alpha(t)$ than in the heave motion $h(t)$, and that the nonlinearity grows with increasing amplitude. Fig. 10 shows a representative phase space diagram of two coexisting LCOs. Between the origin (stable fixpoint) and the first limit cycle (solid), there must be an unstable limit cycle (dashed). The experiments demonstrated that a finite perturbation was necessary to excite the state of the system above a threshold such that the first limit cycle could be reached. The same likewise for the crossover from the first to the second limit cycle.

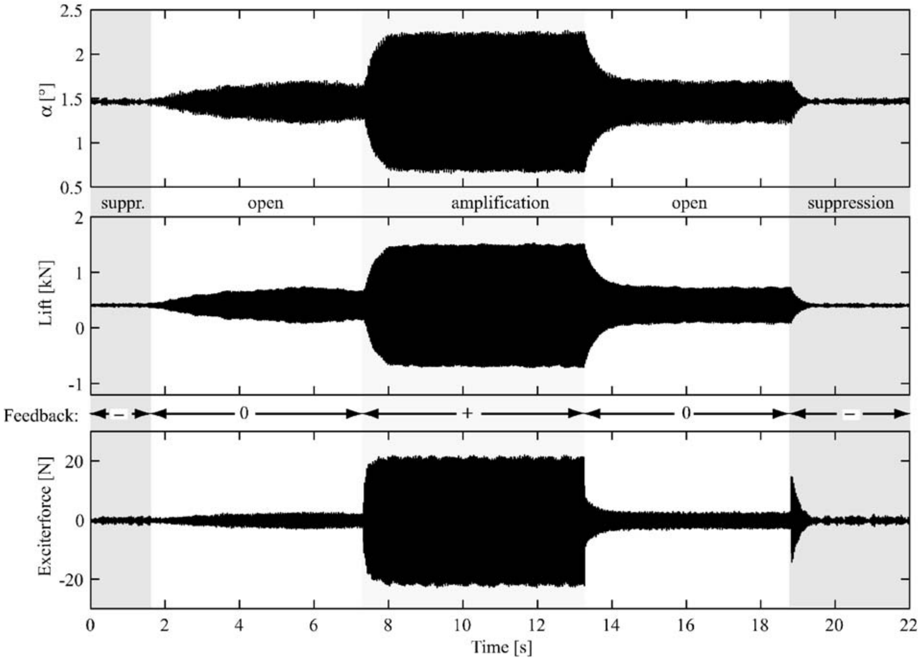

Fig. 6. Demonstration of the control system, which only acts on the heave degree of freedom, on the limit cycle amplitudes (MP 198, Ma = 0.759, Re = 1.40×10^6, $T_\infty = 272$ K, $\alpha_u = 1.46°$).

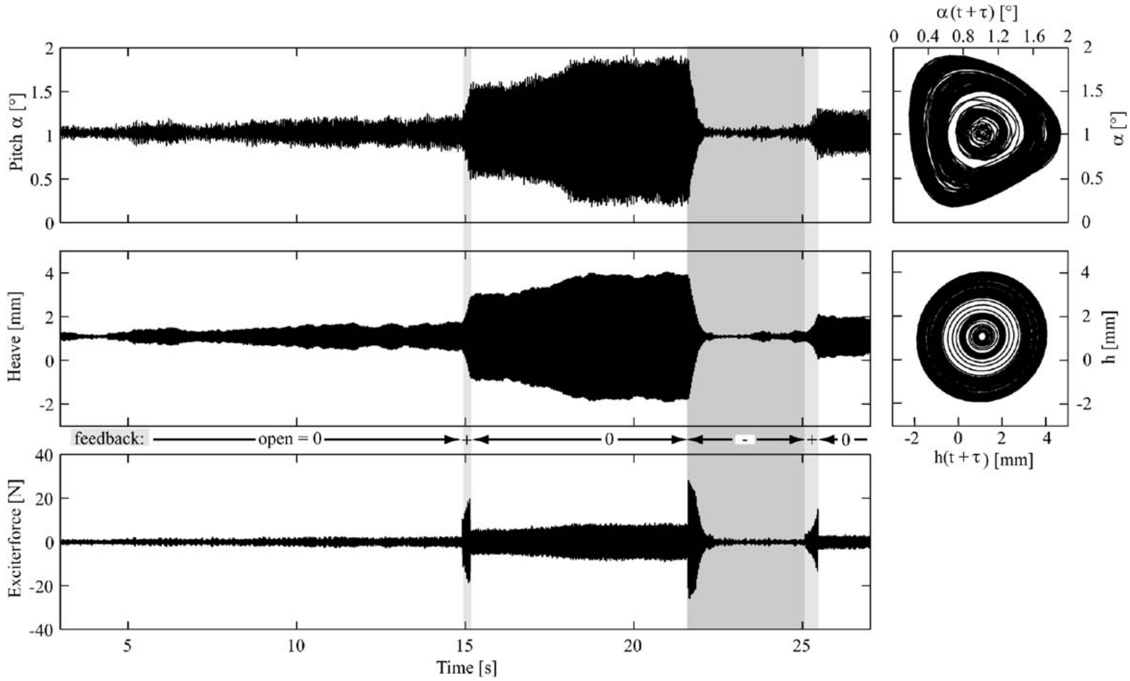

Fig. 7. Demonstration of a jump crossover (subcritical bifurcation), initiated by a small perturbation, i.e. short switch to positive feedback (forced transition, MP 145, Ma = 0.788, Re = 1.97×10^6, $T_\infty = 269$ K, $\alpha_u = 1.02°$).

In Schewe and Deyhle (1996) we have reported that single mode LCOs at free transition can occur near the transonic dip region. Figs. 11 and 12 show LCO behaviour for a model with forced laminar/turbulent boundary-layer transition, demonstrating a crossover from single degree of freedom flutter in pitch to two degree of freedom flutter in pitch and

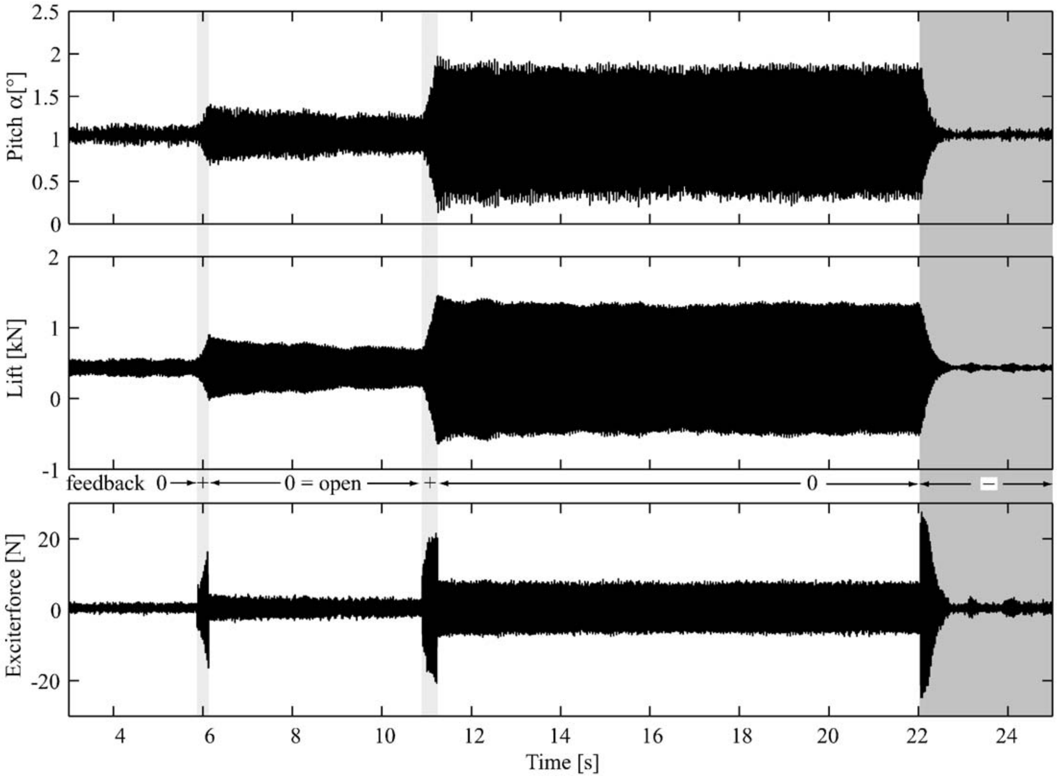

Fig. 8. Demonstration of coexisting limit cycles. Compared to the state in the previous figure, Ma is increased by 0.003. The individual states were fixed via corresponding small disturbances (positive feedback from the control device, MP 146, Ma = 0.791, Re = 1.97×10^6, $T_\infty = 269$ K, $\alpha_u = 1.03°$).

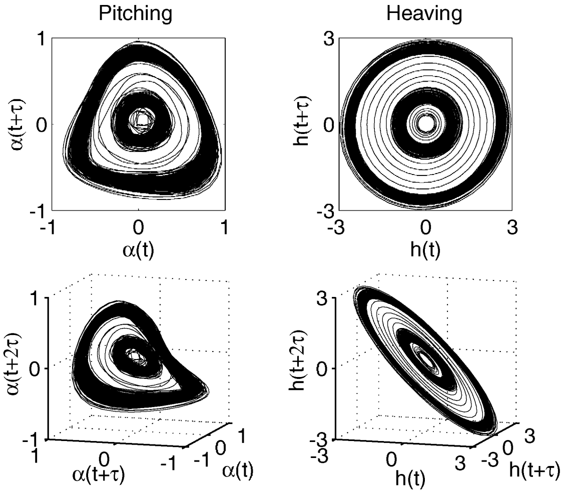

Fig. 9. Phase diagram for the case of a number of limit cycles lying one top of the other (coexisting LCOs) from Fig. 8 (MP 146).

plunge again caused by a very small increase in the Mach number (ΔMa = 0.003). The upper time trace in Fig. 11 shows the spectrogram (short time FFT) of $\alpha(t)$, i.e., the momentary power spectrum depending on time. The crossover is coupled with a discontinuous change in the reduced frequency from $\omega * = 0.3$ to 0.24 and as a consequence a folding of the attractor plane in the phase space (Fig. 12).

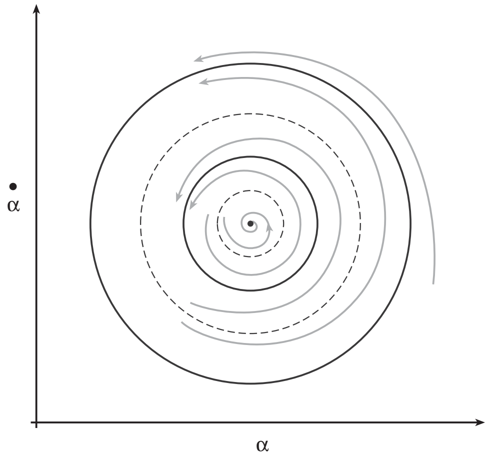

Fig. 10. Schematic representation of coexisting limit cycles (solid: attracting, dashed: repelling).

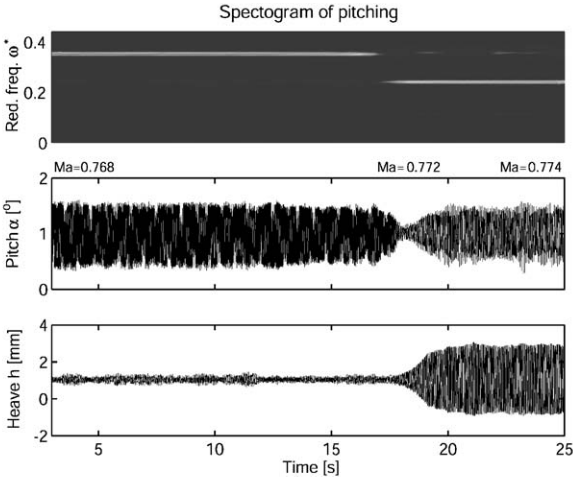

Fig. 11. Crossover from monomode (torsional) to bimodal type (heave and torsion) by a very slight increase of the Mach number $\Delta\mathrm{Ma} = 0.003$. The transition is coupled with a change in the reduced frequency shown by the spectrogram (MP 142, $\mathrm{Ma} = 0.770$, $\mathrm{Re} = 1.93 \times 10^6$, $T_\infty = 271\,\mathrm{K}$, $\alpha_u = 0.99$).

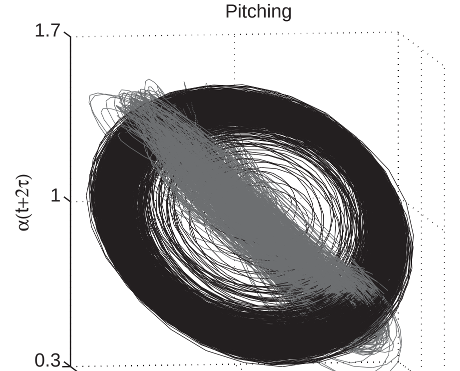

Fig. 12. Phase-space representation of the torsion signal $\alpha(t)$ from Fig. 11. The change of flutter type is reflected in a folding of the plane in which the trajectory travels due to the frequency change. The trajectory is marked grey after the change.

Table 3
Collection of data describing LCOs in particular in Fig. 13 (θ corresponds to growth or decay rate)

MP	Ma_u	α_u (°)	Re ($\times 10^6$)	T_∞ (K)	θ	α_{LCO} (°)	h_{LCO} (mm)	Amp. Ratio	c_l	c_m
Forced transition										
223	0.7600	1.25	2.28	274	0.054	0.07			0.231	−0.054
224	0.7660	1.24	2.29	274	−0.150	0.54	2.00	0.71	0.235	−0.055
225	0.7695	1.22	2.30	274	−0.270	0.66	2.50	0.72	0.239	−0.056
226	0.7695	1.22	2.30	274					0.239	−0.056
227	0.7750	1.21	2.31	273	−0.096	0.78	2.90	0.71	0.241	−0.056
228	0.7793	1.20	2.31	273	−0.053	0.87	3.25	0.71	0.243	−0.056
229	0.7850	1.21	2.32	272	0.000				0.244	−0.055
230	0.7897	1.23	2.33	272	0.047	0.06			0.241	−0.053
Free transition										
77	0.768	1.28	1.7	274		0.20	0.75	0.72	0.272	−0.082
113	0.765	1.36	1.4	278		0.30	0.76	0.76	0.274	−0.074
859	0.820	0.33	2.4	271		0.31	1.72	1.06	0.160	−0.065

Despite the fundamental difficulties associated with the flow-dependent adjusting of the mean angles of attack, we attempted to establish a bifurcation diagram for a situation where the variation of α was very small (only 0.05°) (see Table 3). Fig. 13 shows experimental LCO amplitude data obtained as the transonic dip flutter boundary was crossed starting just before MP 224 (Fig. 4). The first three data points correspond to the time histories in Fig. 4 (cases a, c and d). In the upper graph of Fig. 13, the logarithmic decrement θ depending on Mach number is plotted for the individual cases, which were derived from the exponential part of the decay (case a) or increase (cases c and d). An accurate determination of the stability boundary is thus possible since the Mach number for the zero crossing of the logarithmic decrement can be determined via interpolation. The lower graph of Fig. 13 shows the corresponding LCO amplitudes, which reach values up to $\alpha_{\mathrm{LCO}}=0.87°$ and $h_{\mathrm{LCO}}=3.25$ mm for a dimensionless amplitude ratio $h_{\mathrm{LCO}}/(c\alpha_{\mathrm{LCO}})=0.71$. The reduced frequency of MP 224 is $\omega_F^*=0.244$, which is a typical value for all cases in our experiments when pitching and heaving is involved. The other values can be found in Table 3.

3.3. Limit cycle oscillation test case MP 77 for numerical simulations

The experimental conditions for MP 77 are well suited for numerical investigations since the flow has not yet undergone massive separation. The dimensionless structural-dynamic parameters for this case can be found in Table 1. All other relevant flow and aeroelastic parameters, as well as the observed LCO properties, are listed in Table 2. The self-excited oscillations at MP 77 are characterized by the following properties: It is a limit cycle oscillation in both pitch and plunge with a phase difference of $\Delta\varphi=176°$ between the two degrees of freedom. As such it can also be viewed as a single-degree-of-freedom oscillation with a rotation axis upstream of the elastic axis of the airfoil. In this case the limit cycle amplitudes are $h_{\mathrm{LCO}}=\pm 0.75$ mm for the heaving and $\alpha_{\mathrm{LCO}}=\pm 0.2°$ for the pitching motion. These values are considerably smaller than the numerical results as mentioned in the introduction and in the following discussion. The reduced frequency was determined as $\omega_F^*=0.243$ (for details, see Table 2).

In addition to the pressure distribution in the state of flutter shown in Fig. 14, pressure distributions for forced oscillations of the airfoil (Fig. 16) will be presented in Section 3.4. In this case we attempted to reproduce the essential properties of the flow at MP 77. Fig. 17 also shows a pressure distribution for the fixed model (MP 2084), which represents the steady initial state of MP 77.

Due to wind tunnel wall interference effects in the perforated test-section, either the formulation of appropriate wind-tunnel wall boundary conditions (Castro et al., 2001) or corrections for the flow parameters are necessary. Schewe et al. (2002) mentioned corrections for the Mach numbers and angles of attack, which are based on simple methods and thus have to be regarded with some reservation. For a numerical simulation, it is suggested that one varies the angle of attack and Mach number until the best possible agreement between the measured and calculated pressure distribution is reached. For this procedure, the static states MP 2084 or MP 2086 provide good reference states. In the matching process, emphasis should be placed on the shock location and the observation that the flow at MP 2086 and MP 77 tends to separate at the trailing edge of the suction side. Matching the essential characteristics of the pressure distribution and the flow state is preferable to looking for good agreement in solely the loading coefficients. Weinman and Günther (2002) used this procedure and found best agreement in the corresponding pressure distributions based on

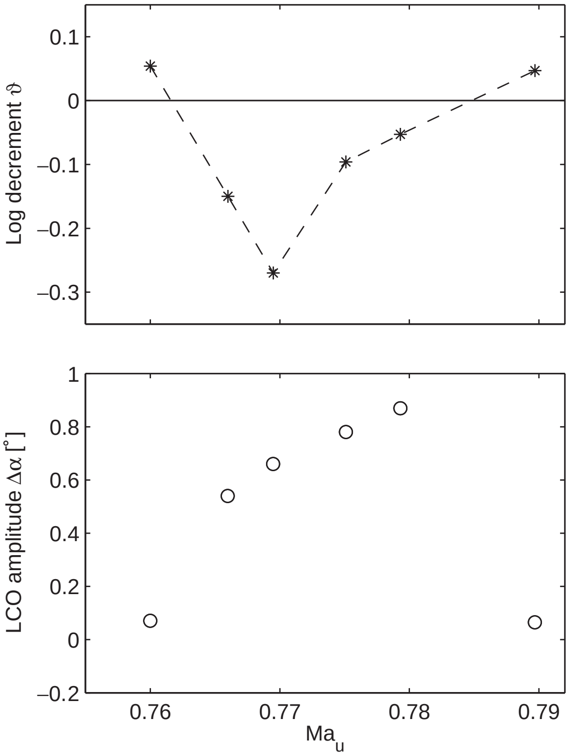

Fig. 13. Logarithmic decrement characterizing the decay or growth rate (upper figure) and LCO amplitude of pitching (lower figure) when the transonic dip is crossed from low to higher Mach number (forced transition).

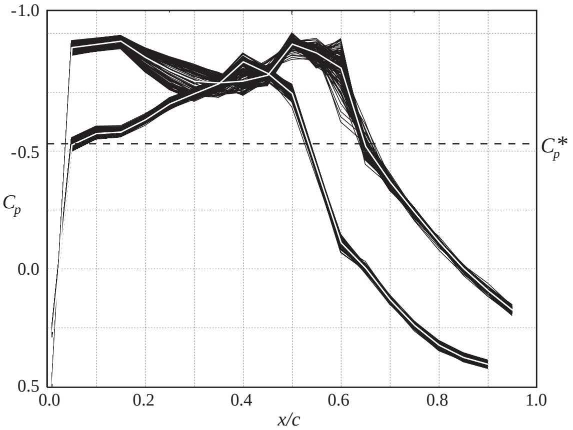

Fig. 14. Superposition of momentary pressure distributions for one oscillation period of MP77. The averaged curve is white (also Fig. 17).

MP 2086, for a “corrected” Mach number and angle of attack of Ma = 0.754 and $\alpha = -0.15°$, respectively. Pressure distributions at MP 77 (i.e., in the state of flutter) were taken in order to gain information pertaining to the mechanism involved in the amplitude-limiting phenomenon.

Fig. 14 shows individual instantaneous pressure distributions, superimposed from one oscillation period. The corresponding average pressure distribution is also shown. This kind of representation gives a visual impression of the fluctuating width of the pressure distribution along the airfoil. The pressure fluctuations on the pressure side of the

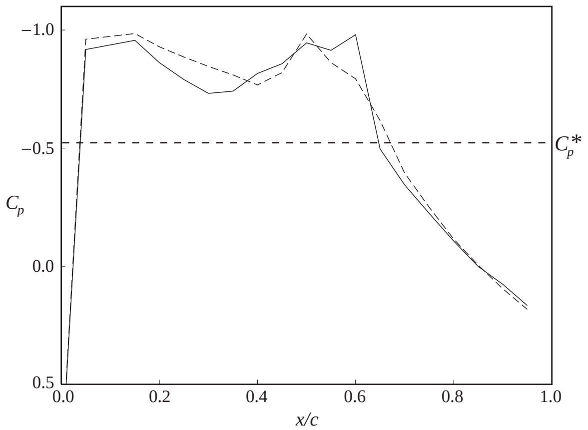

Fig. 15. Two instantaneous pressure distributions at MP 77, taken from Fig. 14, which represent the extreme situations and thereby clearly demonstrate how the shock is divided up. The phase difference in time between both states is $\Delta\varphi = 190°$.

airfoil can be seen to be significantly weaker than those on the suction side. Also the width of the fluctuations is small in the region close to the critical pressure c_p^*. This behaviour is an indication of small shock motion. On the other hand, at the start of the shock ($x/c = 0.6$), the fluctuations are significantly stronger, possibly because of the interaction between the shock and the marginally separated flow region lying below it. Both extreme situations are represented in Fig. 15, which shows two instantaneous pressure distributions taken from the sequence (Fig. 14). The obvious exchange between the waxing and subsequent waning of the shock is a nonlinear process, which is probably coupled with corresponding size changes or pulsations of the marginally separated region (Figs. 14 and 15).

In other words, the oscillations of the strength of the shock, which are coupled with corresponding oscillations of the pressure gradient control the unsteady behaviour of the more or less detached boundary layer. These small-scale effects are quite possibly sufficient to cause amplitude limiting in the flow condition at MP 77. In order to better understand the LCO amplitude-limiting effect, the aerodynamic response to forced harmonic motions has been investigated, in particular its amplitude dependency, and is discussed in the following section.

3.4. Response of the aerodynamic loads to forced oscillations of the airfoil

Fig. 16 shows the steady and unsteady pressure distributions for forced pitching oscillations of MP 2086. The test case most nearly represents the flow conditions at MP 77 ($\alpha = 1.3°$, $\mathrm{Ma} = 0.77$, $\mathrm{Re} = 1.7 \times 10^6$), albeit at a higher Reynolds number ($\mathrm{Re} = 2.3 \times 10^6$).

The unsteady fluid forces were determined by integrating the unsteady pressure distributions. For MP 2086, the flow and forcing parameters are: $\mathrm{Ma} = 0.776$, $p_0 = 60$ kPa, $T_\infty = 273\,\mathrm{K}$, $\alpha_u = 1.25°$, $\omega^* = 0.22$, $f = 30\,\mathrm{Hz}$, amplitude $\Delta\alpha = \pm 0.6°$ (no forced boundary layer transition).

Within the region of the shock, which is shaded in the figure, all values except the real part of $c_{p,\alpha}$ undergo radical change. Downstream of $x/c \approx 0.85$, the r.m.s. value of $c_{p,\alpha}$ on the suction side increases as the trailing edge is approached. This behaviour could indicate a slight trailing-edge separation, which is a characteristic of supercritical airfoils at these Mach numbers. To get an impression as to the comparability of the states, as well as to have a better basis for the test case at MP 77, Fig. 17 again shows the time-averaged pressure distributions and the distributions of their r.m.s. values from MP 2086 (Fig. 16) and from MP 77 (Fig. 14). In addition, to make the motion-induced effects clear, the figure also contains the results of the stationary measurement at MP 2084 ($f = 0\,\mathrm{Hz}$), i.e., with the model at rest, which corresponds to the flow state at MP 2086 ($f = 30\,\mathrm{Hz}$). For the model at rest, it is obvious that the r.m.s. value of the coefficient has a low level all the way to the trailing edge, which implies that the flow remains more or less attached across the stationary model. This behaviour of the r.m.s. value leads to the conclusion that the possible trailing-edge separation mentioned above only becomes noticeable when the model oscillates with a particular amplitude (in our case, with $\Delta\alpha = \pm 0.6°$).

The fact that this effect is not visible in the r.m.s. values at MP 77 could be due to (i) the roughly half as large amplitudes there or (ii) the lower Reynolds number. There is also the possibility that the increase in the r.m.s. value starts downstream $x/c = 0.95$, where we had no pressure tap, and, thus, we could not detect the increase.

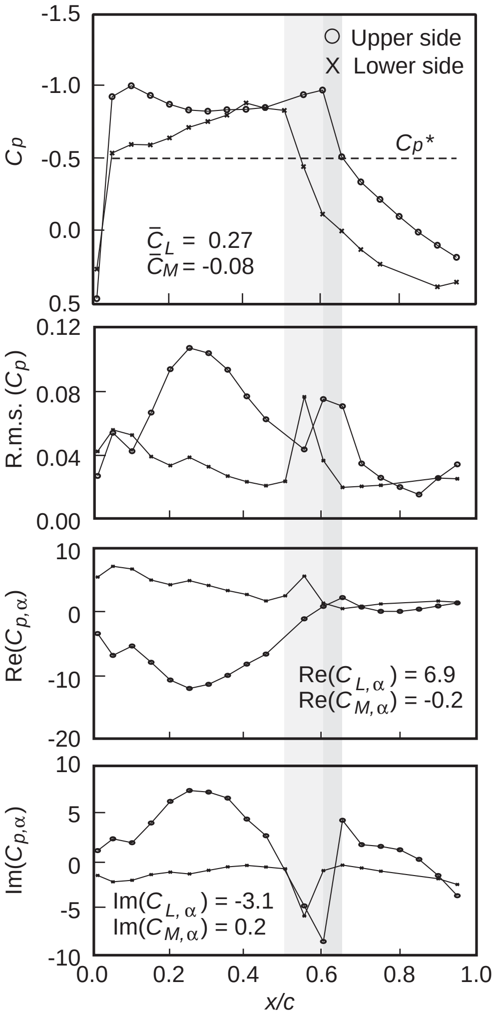

Fig. 16. Example of the results for a pressure-distribution measurement at forced harmonic pitch oscillations. The mean flow state more or less corresponds to the flow of MP77 on the decreasing branch near the transonic dip when $\alpha = 1.25°$ (Ma = 0.77).

In the discussion, we shall return to this observation of the trailing-edge separation and its role as a possible amplitude-limiting effect. Obviously MP 2086 is an interesting case, thus it was selected by Weinman and Günther (2002) as a test case for a numerical simulation of a harmonically pitching airfoil.

Measurements were made at angles of attack of $\alpha = 0.24°$, 1.25° and 3.6° with free transition. In two separate sets of measurements described in Schewe et al. (2002) we determined the coefficients from pressure distributions for forced pitching and heave oscillations as a function of Mach number, which will be the base for the flutter calculations.

The amplitude dependency of the unsteady force coefficients demonstrate the nonlinearity of the aeroelastic system. An example of forced pitching oscillation response is shown in Fig. 18 where the real and imaginary parts of the lift as a function of the oscillation amplitude $\Delta\alpha$ ($\alpha_u = 0.25°$, free transition) are shown for various Mach numbers. These Mach numbers were selected so as to just pass through an unstable region (see Fig. 5), i.e., the lower Mach number Ma = 0.8, and the highest Ma = 0.87, lie in the stable region, while the intermediate Mach numbers lie in the unstable region. It is obvious that for the region 0.8 < Ma < 0.87, where limit cycles were found in the direct flutter experiments, the imaginary part of the coefficient has a high sensitivity to the oscillation amplitude. Such a sensitivity is, however, not observed for the other Mach numbers nor the real part of the unsteady lift.

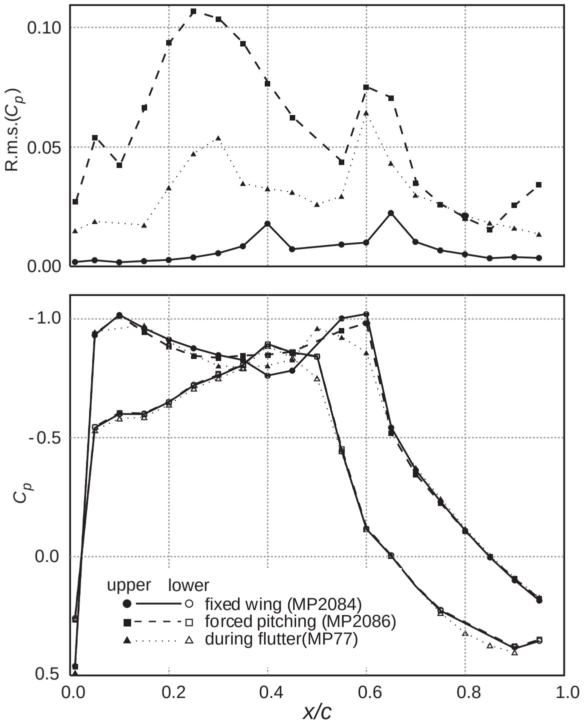

Fig. 17. Compilation of time-averaged pressure distributions and the RMS values, measured at constant inflow conditions about a fixed model and one subjected to forced pitch oscillations. For comparison, values measured during flutter at MP 77 are also included.

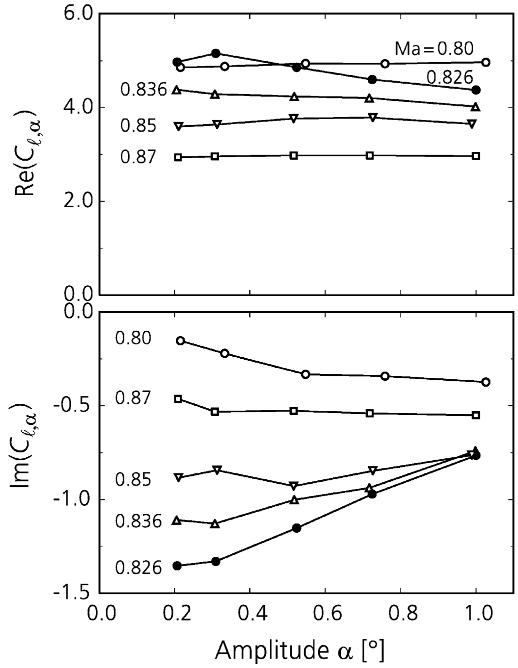

Fig. 18. Amplitude dependence of the unsteady fluid forces (free transition and $\alpha_u = 0.24°$). The results shown are for the lift due to forced torsion oscillations ($f = 20\,\mathrm{Hz}$) as a function of the amplitude at various Mach numbers in the region of the transonic dip.

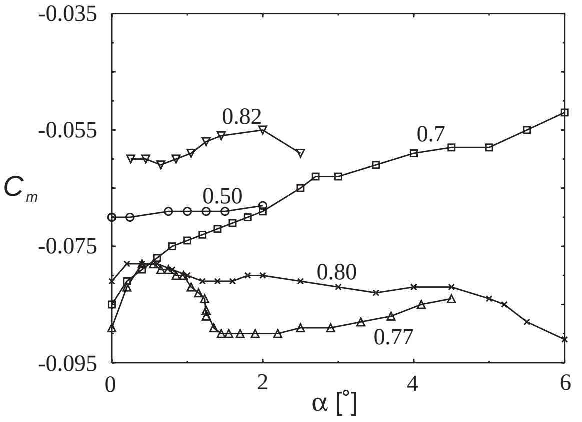

Fig. 19. Moment polars (free transition). Note the negative gradient for Ma = 0.77 around α = 1°—here the torsional instability occurs.

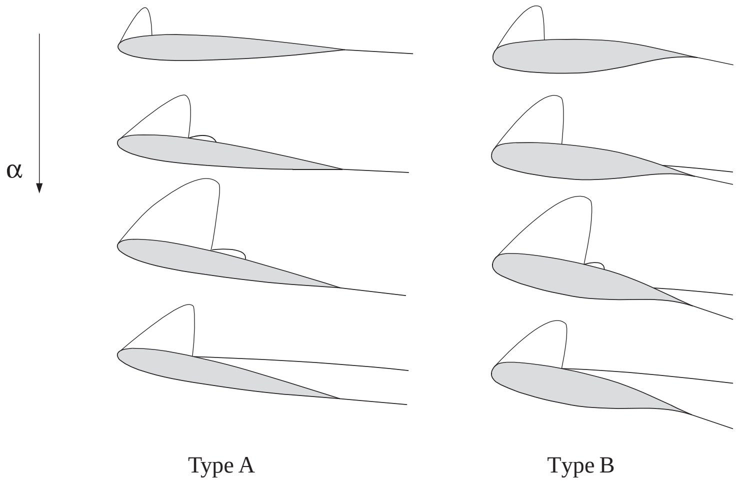

Fig. 20. Types of shock induced separation in flow around a conventional NACA 0012 (type A) and a supercritical airfoil (type B). The main difference is the more important role of the trailing edge separation in case of type B, which is probably responsible for amplitude limitation at relatively low values as observed in the experiments.

4. Discussion

Several manifestations of LCOs were shown in the former chapter. From this the general question arises if the observed small-amplitude limit cycle oscillations in the transonic region were artefacts of our wind tunnel experiments, or if they were truly a natural phenomenon, that could also occur in unbounded flow? Some possible causes for the amplitude limitation could be nonlinearities in the elastic suspension system, transition effects, or wind-tunnel wall interference. But, during flutter measurements in the same test set-up, Schewe et al. (2002) using a conventional NACA 0012 airfoil showed, that the amplitudes grow exponentially up to $\Delta\alpha = \pm 2°$ and $\Delta h = \pm 5\,\text{mm}$ until the mechanical flutter brake was activated. Thus an essential nonlinearity in the springs can be excluded at least up to these amplitudes of oscillation. Concerning the role of the boundary layer transition location, we have demonstrated that LCOs occur regardless of whether the transition is free or fixed. In regard to wind-tunnel wall interference effects, our already mentioned single degree of freedom measurements (Schewe et al., 2002) showed that limit cycles, with amplitudes comparable to those found in the perforated test-section, also appear in the adaptive test-section where interference regarding to the stationary mean flow should be minimal.

In the introduction, we asked if the limitation of amplitudes in the transonic region were always restricted to low values. This question can now be answered with "no", because multiple coexisting limit cycles were found in some of the experiments (Figs. 8–10).

Concerning the question if the transitions from steady to oscillatory state are continuous or discontinuous, we can say that in the presented two examples in Figs. 7–10 the transitions can in fact be discontinuous.

If one looks for the causes in the pure pitching flutter cases (Fig. 11), then as seen in the steady moment polar in Fig. 19, there are already indications of a torsion flutter instability. The moment polar has a negative gradient at $\mathrm{Ma} \cong 0.77$ where pure pitching flutter is observed. A negative gradient $\partial c_m/\partial \alpha < 0$ is an indication of pitching instability. The range for $\partial c_m/\partial \alpha < 0$ extends from about 0.5° to 1.4°, i.e., nearly a value of 1°. This corresponds roughly to the value of the measured limit cycle amplitudes also in case of two degree of freedom oscillation. Although this is a quasi-steady approach, it is conceivable that the onset of the amplitude limitation is roughly related to the locations where the moment polar has a kink, or where the gradient $\partial c_m/\partial \alpha$ has a zero crossing. In general, the nonlinearity in the behaviour of the moment seems to be linked to the amplitude limitation also in the case where pitching and heaving is involved.

Besides the mentioned wind tunnel wall interference effects and changes in the topology of the separated flow, we would like to point out two mechanisms. For both mechanisms we found indications that they have an impact on the amplitude-limiting phenomenon:

(i) The pressure-distribution measurements at MP 77 indicate that interactions between the oscillating shock strength and the coupled pulsations of the marginally separated flow regions beneath the shock could act as amplitude-limiting nonlinearities.

(ii) Another possible cause could be a trailing-edge separation, which we deduced from the significant increase in the r.m.s. value of the pressure fluctuations (Figs. 16 and 17) as the trailing edge was approached. Fig. 20 illustrates the basic differences between flow separations on conventional NACA 0012 and supercritical NLR 7310 airfoils. For the former airfoil, we found no small amplitude ($\alpha < 2^\circ$) limit cycles comparable to those we detected for the latter airfoil (Schewe et al., 2002). One explanation for these findings could be that for increasing Mach number or increasing angle of attack, the type of separation is different. In the case of the conventional airfoil, the first occurrence of separation is mainly shock induced (Fig. 20, type A according to Tijdeman, 1977), whereas for the supercritical airfoil, the process is initiated by trailing-edge separations (Fig. 20, type B), as it occurs in subsonic flow. When the supercritical airfoil undergoes oscillations at certain amplitudes, it is possible that the region of separation induced by the trailing edge and that induced by the shock grow together. It is quite conceivable that the (most probably) anharmonic interplay between the two regions of separation could be responsible for an amplitude limitation.

Both mechanisms should be subject of future experimental and numerical investigations in order to enlighten further the nonlinear aerodynamic phenomena being responsible for the amplitude limitation of LCOs.

Acknowledgements

The authors would like to thank the Federal Ministry for Education and Research for its financial support within the framework of the "Technical Application of Nonlinear Dynamics" program (Project 13N 7172).

We would like to thank Dr. A. Knipfer for participating in the initial stages of the project in the numerical part. Warm thanks are extended to Dr. W.F. King III for translating a great part of the original German-language manuscript as well as for helpful discussions. Thanks are also due to J. Nuhn, who, in particular, was responsible for the data acquisition, J. Berold, who was responsible for the models and the flutter test set-up, and D. Möhle, who was responsible for the hydraulic system and the pitching test set-up. We should also thank Dres. W. Wegner, K. Weinman and G. Langer for many helpful discussions and suggestions, Ms. C. Meyer for the great care with which she finished part of the diagrams.

Finally, we would like to thank the staff of the Transonic Wind Tunnel Göttingen for their patient cooperation in fulfilling all special requests concerning aeroelastic aspects.

References

Bendiksen, O.O., 1989. Nonlinear flutter and divergence in transonic flow. European Forum on Aeroelasticity and Structural Dynamics, Aachen.

Castro, B.M., Ekaterinaris, J.A., Platzer, M.F., 2001. Analysis of the effect of porous wall interference on transonic airfoil flutter. AIAA Paper 2001-2725.

Knipfer, A., Schewe, G., 1999. Investigation of an oscillating supercritical 2d wing in a transonic flow. AIAA Paper 99-0653.

Rivera, J.A., Dansberry, B.E., Bennett, R.M., Durham, M.H., Silva, W.A., 1992. NACA0012 benchmark model experimental flutter results with unsteady pressure distributions. AIAA Paper 92-2396.

Schewe, G., 1991. Force measurements in aeroelasticity using piezoelectric multicomponent transducers. International Forum on Aeroelasticity and Structural Dynamics, Aachen, June 3–6. DGLR Report 91-06.

Schewe, G., Deyhle, H., 1996. Experiments on transonic flutter of a two-dimensional supercritical wing with emphasis on non-linear effects. Proceedings RAeS Conference on Unsteady Aerodynamics, London, UK, 17–18 July.

Schewe, G., Knipfer, A., Mai, H., Dietz, G., 2002. Experimental and numerical investigation of nonlinear effects in transonic flutter. DLR Report IB 232-2002 J01.

Schulze, S., 1997. Transonic aeroelastic simulation of a flexible wing section. AGARD SMP Workshop on Numerical Simulation and Unsteady Aerodynamics and Aeroelastic Simulation. AGARD R-822; 10-1 to 10-20 Aalborg, Denmark.

Tang, L., Bartels, R.E., Chen, P.C., Liu, D.D., 2001. Simulation of transonic limit cycle oscillations using a CFD time marching method. AIAA Paper 2001.

Thomas, J.P., Dowell, E.H., Hall, K.C., 2002. Modelling viscous transonic limit cycle oscillations behaviour using a harmonic balance approach. AIAA Paper 2002-1414.

Tijdeman, H., 1977. Investigations of the transonic flow around oscillating airfoils. Dissertation, Technische Hogeschool Delft, The Netherlands.

Tijdeman, H., Seebass, R., 1980. Transonic flow past oscillating airfoils. Annual Review of Fluid Mechanics 12, 181–222.

Weber, S., Jones, K.D., Ekaterinaris, J.A., Platzer, M.F., 2001. Transonic flutter computations for the NLR 7301 supercritical wing. Aerospace Science and Technology 5, 293–304.

Weinman, K., Günther, G., 2002. personal communication.

Zimmerman, H., Weissenburger, J.T., 1964. Prediction of flutter onset speed based on flight testing at subcritical speeds. Journal of Aircraft 1, 190–202.

Zwaan, R.J., 1979. Summary of data required for the AGARD SMP activity "Standard Aeroelastic Configurations"—two-dimensional configurations, MP 79015 U, NLR.